Geometrical optimization of microstripe arrays for microbead magnetophoresis

Henriksen, Anders Dahl; Rozlosnik, Noemi; Hansen, Mikkel Fougt

Published in:
Biomicrofluidics

Link to article, DOI:
10.1063/1.4934679

Publication date:
2015

Document Version
Publisher's PDF, also known as Version of record

Geometrical optimization of microstripe arrays for microbead magnetophoresis

Anders Dahl Henriksen, Noemi Rozlosnik, and Mikkel Fougt Hansen

Citation: Biomicrofluidics **9**, 054123 (2015); doi: 10.1063/1.4934679
View online: http://dx.doi.org/10.1063/1.4934679
View Table of Contents: http://scitation.aip.org/content/aip/journal/bmf/9/5?ver=pdfcov
Published by the AIP Publishing

Geometrical optimization of microstripe arrays for microbead magnetophoresis

Anders Dahl Henriksen, Noemi Rozlosnik, and Mikkel Fougt Hansen[a)]
Department of Micro- and Nanotechnology, Technical University of Denmark, DTU Nanotech, Building 345 East, DK-2800 Kongens Lyngby, Denmark

(Received 2 September 2015; accepted 14 October 2015; published online 21 October 2015)

Manipulation of magnetic beads plays an increasingly important role in molecular diagnostics. Magnetophoresis is a promising technique for selective transportation of magnetic beads in lab-on-a-chip systems. We investigate periodic arrays of exchange-biased permalloy microstripes fabricated using a single lithography step. Magnetic beads can be continuously moved across such arrays by combining the spatially periodic magnetic field from microstripes with a rotating external magnetic field. By measuring and modeling the magnetophoresis properties of thirteen different stripe designs, we study the effect of the stripe geometry on the magnetophoretic transport properties of the magnetic microbeads between the stripes. We show that a symmetric geometry with equal width of and spacing between the microstripes facilitates faster transportation and that the optimal period of the periodic stripe array is approximately three times the height of the bead center over the microstripes. © *2015 AIP Publishing LLC*.
[http://dx.doi.org/10.1063/1.4934679]

I. INTRODUCTION

Magnetic beads play an increasingly important role in modern scientific and pharmaceutical molecular diagnostics and are used to spatially manipulate and mark biological targets.[1,2] The precise and selective control of magnetic beads is attracting large interest and is seen as a promising candidate for lab-on-a-chip sample preparation.[3] Magnetic beads in combination with magnetic forces have long been used for concentration and purification of biological targets.[4,5] This is most easily done by trapping the beads using a strong magnetic field gradient.[4,6,7] To obtain high throughput, magnetic forces have also been used to separate magnetic beads in a fluid flow.[8–11] Cleanroom fabrication has been used to fabricate chips with hard ferromagnetic materials in the micro regime that show a great reproducibility for purifying magnetic beads.[12–14] Moreover, arrays of cobalt micro-magnets in combination with a rotating external magnetic field have been used for the magnetophoretic transportation of magnetic beads, and their ability to separate beads with different magnetophoretic mobilities by tuning the frequency of the applied magnetic field has been demonstrated.[15–17]

Previously, we have shown that magnetic beads can be selectively transported between stripes on a chip with periodic arrays of long exchange-biased permalloy microstripes using a rotating external magnetic field.[18] Recently, the use of a continuous film with a periodic array of exchange-biased stripes with alternating magnetization orientations induced by ion bombardment was also presented.[19] Common for these studies is that the interaction between the spatially varying magnetic field from the stripes and a weak temporally rotating external field can create a magnetic wave with a point of minimum magnetic energy that will sweep across the chip and drag the magnetic beads along. This magnetophoretic manipulation requires no electrical contacts to the chip and no pumps and valves. Further, the structures are fabricated using a single mask step. This opens the possibility for low-cost batch manipulation of

[a)]Electronic mail: Mikkel.Hansen@nanotech.dtu.dk

magnetic beads and for batch screening of magnetic compounds in a lab-on-a-chip environment. The previous studies, however, have not systematically considered and optimized the geometry of the stripes.

Here, we study the influence of the microstripe geometry on the magnetophoresis transportation properties to determine the optimal geometries for transportation and separation of magnetic beads with different magnetophoretic mobilities. We systematically investigate experimentally and in numerical simulations thirteen designs with different periodic microstripe array geometries and measure their magnetophoresis properties when used to transport magnetic microbeads. We show that a symmetric geometry of stripes with equal width and spacing is optimal and that the optimal spatial period of the periodic stripe structure is approximately three times the height from the stripe plane to the bead center.

II. THEORY

A. Magnetophoretic mobility

We used Dynabeads® M-270 Carboxylic Acid beads in our experiments. These beads are superparamagnetic and thus, in a weak magnetic field, the magnetization is proportional to the applied field $\mathbf{M}_{\text{bead}} = \chi \mathbf{H}$, where χ is the effective magnetic susceptibility of a bead and $\mathbf{H}$ is the magnetic field in the absence of the bead. The induced magnetization gives rise to a magnetic force[20]

$$\mathbf{F}_{\text{m}} \simeq \mu_0 \mathcal{V} \chi (\mathbf{H} \cdot \nabla)\mathbf{H} = \frac{1}{2}\mu_0 \mathcal{V} \chi \Delta(\mathbf{H}^2), \tag{1}$$

where $\mathcal{V}$ is the volume of the bead and μ_0 is the permeability of free space. This magnetic force drags the bead toward the point of maximum magnetic field strength. A bead moving at a velocity $\mathbf{v}$ with respect to the surrounding fluid (which is at rest in this work) is further subject to a Stokes drag force[21]

$$\mathbf{F}_{\text{d}} = -6\pi\eta r \mathbf{v} f_{\text{D}}. \tag{2}$$

Here, η is the fluid viscosity, r is the bead radius, and $1 \leq f_{\text{D}} \leq \frac{256}{83}$ is a correction coefficient if the bead is in the vicinity of a wall given by[22]

$$f_{\text{D}} = \left(1 - \frac{9}{16}\left(\frac{r}{r+z_{\text{w}}}\right) + \frac{1}{8}\left(\frac{r}{r+z_{\text{w}}}\right)^3 - \frac{45}{256}\left(\frac{r}{r+z_{\text{w}}}\right)^4 - \frac{1}{16}\left(\frac{r}{r+z_{\text{w}}}\right)^5\right)^{-1}, \tag{3}$$

where z_{w} is the distance from the bead-perimeter to the wall. In the case of a micro sphere and negligible inertia, the bead motion can be assumed to be at steady state and thus the magnetic force is balanced by the drag force such that the total force is zero. This results in a bead velocity of

$$\mathbf{v} = \mu_0 \xi \nabla(|\mathbf{H}|^2), \tag{4}$$

where we have defined the magnetophoretic mobility

$$\xi = \frac{\mathcal{V}\chi}{12\pi\eta r f_{\text{D}}}. \tag{5}$$

The above equation shows that the bead velocity is proportional to the susceptibility of the bead and inversely proportional to its drag coefficient. The Dynabeads® M-270 beads have a nominal diameter of $2r = 2.8\,\mu$m, and their effective magnetic susceptibility has been measured by Fonnum *et al.* to $\chi = 0.76$.[23] Using $\eta = 1.002$ mPa s and setting $z_w = 0$ (contact), we obtain $\xi_{\text{M-270}} = 54\ \mu\text{m}^2/\text{Pa s}$.

B. Magnetic field from stripe array

The magnetic beads are moved by combining the spatially varying field from the periodic array of stripes with a rotating external magnetic field. The stripes are assumed to be infinitely long in the y-direction and to be magnetized along the x-direction as illustrated in Fig. 1(a). The magnetic field from the array of stripes, $\mathbf{B}_{\mathrm{s},}$ can be found by converting the magnetization to surface currents and using the Ampère-Maxwell law for the magnetic potential. The procedure is described in detail in the supplementary information of Henriksen *et al.*[24] Calculating $\mathbf{B}_{\mathrm{s}} = (B_{\mathrm{s},x}, B_{\mathrm{s},z})$, we find that the y-component of the magnetic field from the stripes, $B_{\mathrm{s},y}$, is zero while the $B_{\mathrm{s},x}$ and $B_{\mathrm{s},z}$ components resemble those from a bar magnet with field lines going from one end to the next and with strong gradients close to the edges. This is illustrated in the surface plot in Fig. 1(a). In this figure, the stripe width w, the spacing s, the period $\lambda = w + s$, and the ferromagnetic layer thickness t_{FM} are also defined. If one includes more stripes and brings them closer together, the magnetic field from one pole (a face of a stripe with non-zero normal component of $\mathbf{M}$) extends towards both neighboring poles with the majority of the field

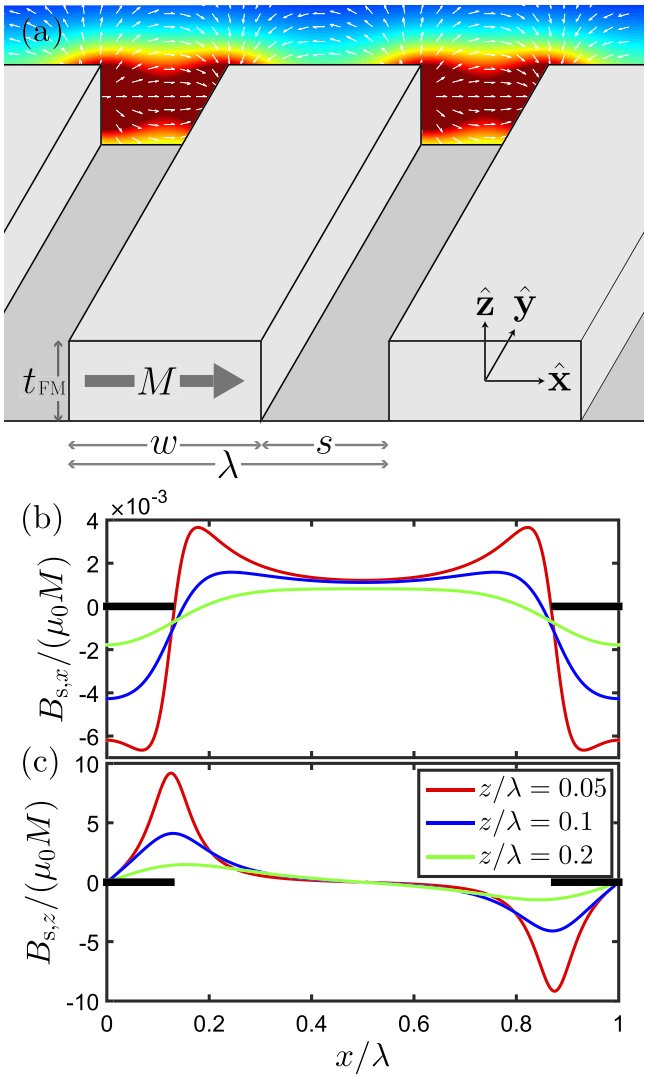

FIG. 1. (a) Illustration of the periodic stripe system, the used coordinate system, and the magnetic field, $\mathbf{B}_{\mathrm{s},}$ from the array of magnetic stripes. Red colors indicate a high field magnitude. (b) x-component and (c) z-component of the magnetic field from the stripes for different height-to-period ratios. The black bars indicate the location of the stripes. The calculations were carried out for a ferromagnetic layer of thickness $t_{\mathrm{FM}}/\lambda = 0.003$ and a volume magnetization M.

lines ending at the nearest opposite pole. When two opposite poles approach each other, the magnetic field lines are confined between the poles creating a stronger but also more localized magnetic field and magnetic field gradient.

Depending on the geometry, the magnetic field from the stripes, $\mathbf{B}_{s,}$ can have three shapes, which can be distinguished in the different modes of $B_{s,x}$. When $z/\lambda \geq 0.2$, the distance from a bead to neighboring poles is comparable and the fields from several poles overlap. This creates a weak but approximately sinusoidally varying magnetic field with $B_{s,x}$ being strong between the poles and $B_{s,z}$ being strong above the poles, see Fig. 1(b). Conversely, for $z/\lambda \leq 0.1$, the distance to one pole is smaller than the distance to the rest of the poles. In this case, the field experienced by a bead is stronger, but also highly localized, with a large magnetic field and magnetic field gradient close to the poles and with regions between poles with a much smaller gradient. Here, $B_{s,x}$ is strong in the vicinity of the poles because of the localized nature of the field. Thus, the number of $B_{s,x}$ maxima between two poles can vary from one at each pole to one between two poles depending on the value of z/λ. If the stripe width is different from the spacing ($w \neq s$), this shift happens at different heights meaning that the magnetic field may have two, three, or four maxima for $|B_{s,x}|$ for one period, see Fig. 1(b).

C. Magnetic bead motion on stripe array in rotating magnetic field

The magnetic beads are attracted towards the points of maximum magnetic field strength. Figure 2 shows how the spatially varying magnetic field can be combined with a rotating external field to continuously move the magnetic beads along the positive x-direction. The magnetic field from the stripes spatially changes from being parallel to $\hat{\mathbf{z}}$ above the stripe north face to anti-parallel above the stripe south face. Thus, by letting the external field rotate from $-\hat{\mathbf{z}}$ to $\hat{\mathbf{z}}$,

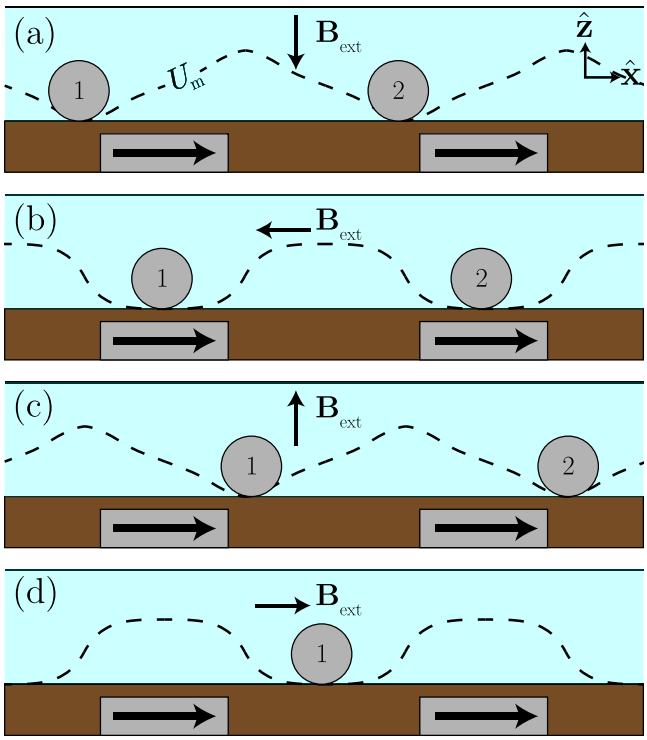

FIG. 2. Illustration of concept for magnetic bead magnetophoresis across the array of magnetized stripes. The stripes are magnetized in the x-direction and extend to infinity in the y-direction. The superposition of the external magnetic field that rotates in the xz-plane and the static field from the magnetized stripes creates an energy minimum that travels across the stripe array along the positive x-direction and drags the beads (labeled as 1 and 2) along. The potential energy landscape for a bead for each field condition is illustrated with the dashed curve.

the point of maximum field strength moves from the south face to the north face and so will the bead.

It should be noted that beads located at the point, where the external magnetic field in the vertical direction has a direction opposite to that of the field from the stripes (e.g., over the north pole in Fig. 2(a)), may be located at a point of minimum field strength and hence experience a lift force in the positive z-direction. This may be the case when the external field has the same magnitude as the field from the stripes at the bead location.

The periodic array of magnetic microstripes (Fig. 1) creates a periodic magnetic field in the xz-plane. Periodic fields are well suited for bead transportation as they can supply a strong magnetic gradient over infinite distances. Due to the complex and alternating nature of the magnetic field from the stripes, the bead velocity oscillates as the function of position and time, with the bead motion being fastest when approaching the stripe edges. A bead can at most move one spatial period per rotation of the external field. Yellen *et al.* described this motion as being phase-locked.[15] For comparing velocities in different geometries, we consider the normalized time-averaged velocity

$$V = \frac{\langle v \rangle}{\lambda f}, \tag{6}$$

where $\langle v \rangle$ is the time-averaged velocity and f is the rotational frequency of the external field. In this way, any bead will have a normalized velocity $0 \leq V \leq 1$, with $V = 1$ corresponding to phase-locked behavior.

As the bead velocity is proportional to the magnetophoretic mobility, Eq. (4), a bead with twice the magnetophoretic mobility is able to travel the spatial period, λ, in half the time. For a rotating field, this implies that the bead is able to be transported in a field with twice the rotational frequency. When the rotational frequency of the external field becomes too high for a bead to follow, it starts to move with $V < 1$ before becoming stationary ($V = 0$).[16] Thus, there is a maximum and critical frequency, $f_{V=1}$, up to which a bead can follow the traveling magnetic wave with phase-locked velocity. The corresponding maximum magnetic bead velocity is $f_{V=1} \cdot \lambda$.

The expected bead velocity in a given system was calculated as follows: First, the magnetic field from the stripes was calculated using the expressions given by Henriksen *et al.*[24] This was superposed with the rotating external magnetic field and, with magnetophoretic mobility, $\xi_{\mathrm{M-270,}}$ used in the equation of motion, Eq. (4) to calculate the bead velocity. The equation of motion was then numerically integrated until a periodic bead motion was observed. To obtain the maximum velocity, $f_{V=1} \cdot \lambda$, the phase-locked frequency was determined using bisection.

We note that the geometry of the stripes and hence the magnetic force is invariant to translation in the y-direction. The results presented below obtained without a fluid flow therefore also apply for a system with a fluid flow along the y-direction as the equation of motion is decoupled in the x- and y-directions. If a fluid flow is applied along the x-direction, the full equation of motion, including the fluid flow, has to be solved.

III. EXPERIMENTAL

A. Chip design and fabrication

The chips with magnetic microstripes were fabricated in a single lift-off process. The stripes were patterned in photoresist using UV lithography. The exchange-biased permalloy stacks had the nominal composition Ta(3)/$Ni_{80}Fe_{20}$(5)/$Mn_{80}Ir_{20}$(10)/$Ni_{80}Fe_{20}$(10)/$Mn_{80}Ir_{20}$(10)/Ta(3) (thicknesses in nm). The stack was sputtered in a K. J. Lesker Co. model CMS 18 magnetron sputtering system and defined by lift-off of the remaining photoresist. The easy direction was defined along the x-direction by depositing the stripes in a magnetic field of 20 mT. The 5 nm thick bottom Ni-Fe layer was included to ensure proper growth conditions for the bottom antiferromagnetic Mn-Ir layer. The 10 nm thick top Ni-Fe layer was pinned on both the top and the bottom by antiferromagnetic layers to maximize the exchange-biasing and hence the

stability of its magnetization orientation in external magnetic fields. Finally, the wafer was covered with 90 nm of sputtered SiO_2. This coating protected the magnetic stack from corrosion during experiments.

Three sets of chips with different stripe array geometries were fabricated: *Symmetric* geometries with $w = s = 5$, 6, 8, and 10 μm, *Constant spacing* geometries with $s = 5\,\mu$m and $w = 2$, 4, 5, 6, 8, and 10 μm, and *Constant period* geometries with $\lambda = w + s = 10\,\mu$m and $w = 2$, 4, 5, 6, 8, and 10 μm. Note that the geometry $w = s = 5\,\mu$m was in all three groups and thus a total of thirteen different geometries were fabricated. Each chip had a dimension of $6 \times 6\,\text{mm}^2$. The fabricated structures showed a magnetic behavior typical for exchange-biased thin films with a field-offset hysteresis loop. For all geometries listed above, the magnetization was close to constant for applied magnetic flux densities in the x-direction of 5 mT and below. Hysteresis loops measured for the symmetric designs are shown in the supplementary Figure S1.[25] This figure also includes a measurement for a symmetric stripe geometry with $w = s = 2\,\mu$m (not included in the study below), where the shape anisotropy of the stripe dominates such that the stripes are no longer magnetized along the x-direction.

B. Experimental setup

The bead magnetophoresis measurements were performed in a home-built setup. A PMMA chip holder defined a simple fluid system for bead injection, where the chip was placed in a well with an inlet and an outlet on each side. The well was sealed using a polydimethylsiloxane (PDMS) gasket. The fluid system had a depth of 1 mm and a volume of 50 μl. The magnetic beads were actuated by two Helmholtz coils of different sizes, see Fig. 3. The Helmholtz coils provided a homogeneous hysteresis free rotating magnetic field of

$$\mathbf{B}_{\text{ext}} = B_0[\cos(2\pi tf)\hat{\mathbf{x}} - \sin(2\pi tf)\hat{\mathbf{z}}], \tag{7}$$

where B_0 was the magnitude of the applied magnetic flux density. The Helmholtz coils were driven by Kepco BOP 20–10M and Kepco BOP 50–8M current amplifiers. The electromagnets and timing of the image acquisition were controlled in LabView using a National Instruments PCI 6723 card. The bead motion was captured by a Unibrain Fire-i 785c camera attached to a microscope with a 10× magnification lens. The camera was hardware triggered from Labview to take a picture when $\mathbf{B}_{\text{ext}}$ was along the positive z-direction (Fig. 2(c)).

C. Experimental procedure

The fluid system was initially filled with Milli-Q water. Dynabeads M-270 Carboxylic Acid (ThermoFisher Scientific) were 100× diluted from their stock concentration in milli-Q

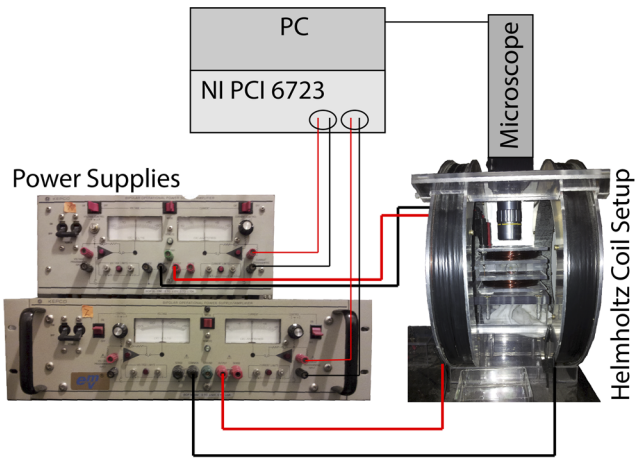

FIG. 3. Illustration/picture of the experimental setup.

water to 2×10^7 beads/ml and subsequently injected. Experiments were carried out without blocking of the chips and the fluidic system and without addition of detergents to the fluids. After injection, the beads were allowed to sediment for two minutes after which the actuation experiment was initiated. All experiments were carried out without a fluid flow in the system. During actuation, the Helmholtz coils provided a homogeneous rotating field with $B_0 = 5\,\mathrm{mT}$ at a frequency f. This value of B_0 was used, as it was strong enough to overcome the magnetic field from the stripes at their edges but still weaker than the exchange-bias field pinning the magnetization of the Ni-Fe layer.

To determine the maximum magnetophoretic bead velocity, the frequency of the rotating magnetic field was increased from $f = 1\,\mathrm{Hz}$ to $30\,\mathrm{Hz}$ in steps of $1\,\mathrm{Hz}$. For each frequency, eleven field cycles were performed, and correspondingly a video of eleven frames was recorded for later analysis.

D. Data analysis

The analysis of the captured videos was done by a particle tracking algorithm written in Matlab. First, the beads were identified in all frames. This was done by converting to gray scale, examining whether each pixel was in a local area of darker luminescence and clustering the darker pixels into beads. When all bead locations were identified, the algorithm compared the position of each bead in the given frame to that in the previous frame. If a bead had not moved, it was categorized as stationary. If a bead had moved one spatial period, it was assumed to be phase-locked. When a bead could not be traced from one image to the next, it was marked as a bead that could not be categorized and it was not counted in the data. For example, a new bead that entered an image during an experiment would be labeled as not categorized and not be counted until it had been observed in three subsequent images. An example of a frame, with identified and categorized beads, is given in the inset of Fig. 4. The beads were tracked throughout the video, and for each bead tracked through three frames or more, the frame-averaged normalized bead velocity V was calculated. From these normalized velocities, the percentage of beads, $P_{V\geq\frac{1}{2}}$, with $V > \frac{1}{2}$ as well as its standard deviation were calculated. The beads with $V \geq \frac{1}{2}$ were considered phase-locked whereas those with $V < \frac{1}{2}$ were considered stationary. We remark that stationary beads generally did not block the motion of other beads. We believe that this is due to the fact that there is no magnetic force from the stripes acting on the beads along the stripes and hence there the magnetic beads can easily change their path to pass a small obstacle.

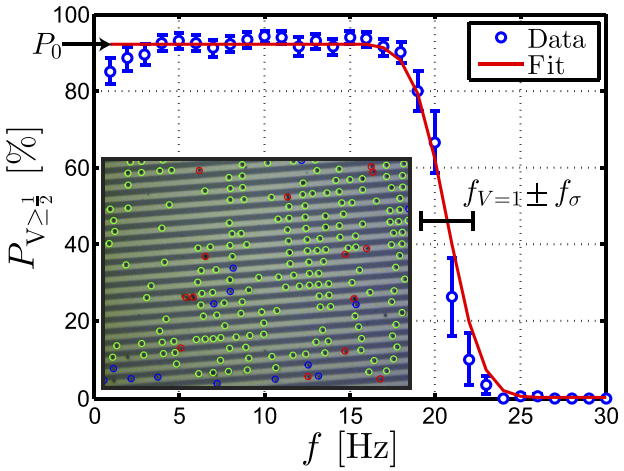

FIG. 4. Example of a frequency sweep for a stripe geometry with $w = s = 6\,\mu\mathrm{m}$. The line is a fit of the binomial distribution with probability given by Eq. (8) to the data with the parameters given in Table I for chip 2. The inset shows an example of an analyzed frame with stationary beads (red circles), phase-locked beads (green circles), and beads that could not be categorized (blue circles).

The magnetic beads contain different amounts of magnetic material and their magnetophoretic mobilities, therefore, vary. To account for this, we assume that the magnetophoretic mobility is normal distributed. As discussed, the magnetophoretic mobility, ξ, is proportional to the critical frequency $f_{V=1}$, and thus, a normal distribution of the magnetophoretic mobility will result in a normal distribution of critical frequencies. Each bead in the filmed ensemble of magnetic beads should thus follow the rotating field with a probability given by

$$\mathcal{P}_{V=1}(f|f_{V=1},f_\sigma,P_0) = \frac{P_0}{2}\mathrm{erfc}\left(\frac{f_{V=1}-f}{\sqrt{2}f_\sigma}\right), \tag{8}$$

where f is the frequency of the rotating external field, $f_{V=1}$ and f_σ are the mean and standard deviation of the normal distribution of the critical frequencies for phase-locked motion, and erfc is the complementary error function. The fitting parameter P_0 is the percentage of mobile magnetic beads, and it was introduced to account for a small fraction of magnetic beads that were stuck on the sensor surface (5%–10%).

Knowing the probability for each bead to follow the rotational field, the number of moving beads should be binomially distributed. As f increases, the binomial distribution shifts from favoring phase-locked beads to favoring stationary beads.

IV. RESULTS

A. Chip-to-chip reproducibility

To check the reliability and reproducibility of the measurement procedure, experiments on the same magnetic geometry were repeated on three different chips from different locations on the fabricated wafer. Figure 4 shows one of these frequency sweeps. The line is a fit of Eq. (8) to the measured values of $P_{V\geq\frac{1}{2}}$ with $f_{V=1}$, f_σ and P_0 as free parameters. A gradual decrease of $P_{V\geq\frac{1}{2}}$ around $f=f_{V=1}$ is observed in accordance with the idea of a normal distribution of magnetophoretic mobilities. Table I gives the values for the above parameters obtained from frequency sweeps corresponding to that in Fig. 4 on three different chips from the same wafer. The measured critical frequencies $f_{V=1}$ varied 1.6 Hz or 8% between the chips. The variation is small and can mainly be attributed to a variation of the total thickness of the permalloy layer between the investigated chips that were taken from different locations on the fabricated wafer. The results demonstrate the reproducibility of the experimental results. The variation between repeated experiments on the same chip was negligible (not shown).

B. Maximum magnetophoretic velocity vs. geometry

To understand the influence of the magnetic stripe geometry on the magnetophoresis velocity, we measured the maximum bead velocity for the presented thirteen different geometries. Figure 5(a) shows $f_{V=1}\cdot\lambda$ vs. w for symmetric stripe geometries ($w=s$). The experimentally obtained values of $f_{V=1}$ were obtained from experiments like that in Fig. 4, and the simulated values were obtained as described in Sec. II C. In Fig. 5(a), the maximum measured bead velocity is found to decrease for increasing period ($w\geq 5\,\mu$m). Further, the simulations predict an optimal period around $\lambda=2w\approx 5\,\mu$m and hence that the maximum magnetophoretic velocity decreases monotonically for increasing deviations of w from $w\approx 2.5\,\mu$m.

TABLE I. Fitting parameters for measurements on three different chips with the same geometry ($w=s=6\,\mu$m).

	$f_{V=1}$ (Hz)	f_σ (Hz)	P_0 (%)
Chip 1	20.5(1)	1.5(1)	93(1)
Chip 2	20.7(3)	1.6(2)	92(1)
Chip 3	22.1(1)	1.2(1)	94(1)

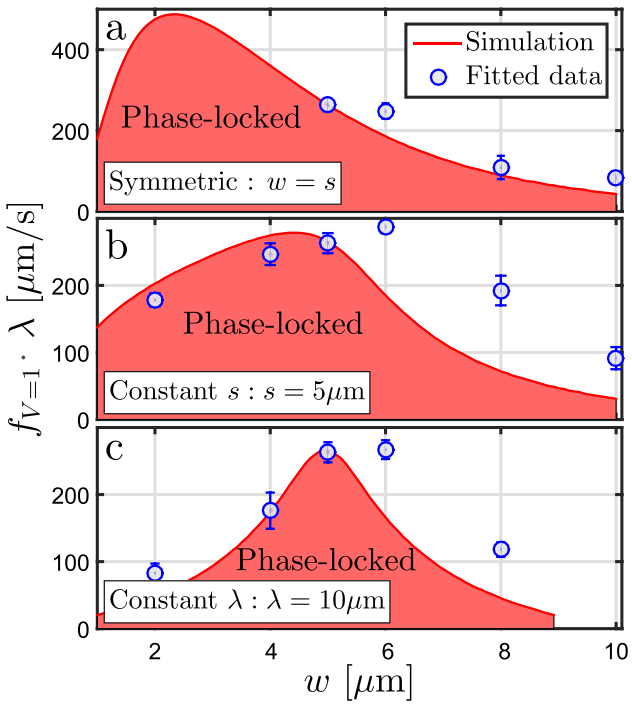

FIG. 5. Maximum magnetophoretic velocity as function of the stripe width w for stripe geometries with (a) equal width and spacing, (b) constant spacing, and (c) constant period. The blue circles are measured velocities, and the red areas are simulated using $\xi_{\text{M-270}} = 54\ \mu\text{m}^2/\text{Pa s}$ with no fitting parameters. The error bars correspond to $\pm f_\sigma \cdot \lambda$.

Figure 5(b) shows $f_{V=1} \cdot \lambda$ vs. w for stripe geometries with a constant spacing of $s = 5\ \mu$m. The results of the constant spacing geometries (Fig. 5(b)) are comparable to the symmetric, $s = w$, geometries (Fig. 5(a)) but both the simulated and measured velocities decrease for decreasing w when $w < 5\ \mu$m. The symmetric and constant spacing geometries have the single optimum $w = s = 5\ \mu$m geometry in common. For $w \geq 5\ \mu$m, the transportation properties seem to follow the same pattern of decreasing maximum velocity with increasing w. A geometry with $w = 10\ \mu$m and $s = 5\ \mu$m has approximately the same period as a geometry with $w = 8\ \mu$m and $s = 8\ \mu$m. Theoretically, the maximum velocity is significantly lower for the asymmetric geometry, but experimentally, the maximum magnetophoretic velocities are approximately the same for the two geometries.

Figure 5(c) shows $f_{V=1} \cdot \lambda$ vs. w for a geometry with a constant period of $\lambda = 10\ \mu$m. For these designs, simulations and measurements agree and the highest magnetophoretic velocity is obtained for $w \approx s \approx \lambda/2 = 5\ \mu$m.

V. DISCUSSION

A. Geometry optimization

Magnetophoretic transportation is possible in all our micro-sized geometries, but the maximum obtainable velocities vary significantly with geometrical parameters. Figure 6 summarizes the influence of the geometry for the transportation of M-270 beads as obtained from simulations.

The measured and simulated data in Figs. 5(c) and 6 show that, for constant other parameters, bead transportation is easiest when the width and spacing are equal, $w = s$. In this case, $B_{s,x}$ and $B_{s,z}$ show a high degree of symmetry around the magnetic poles, which is optimal for transporting magnetic beads using a rotating field. Generally, bead transportation is easier when the magnetic field from the stripes has a sinusoidal-like variation and this is better achieved for a symmetric geometry. When the geometry is asymmetric ($w \neq s$), the magnetic bead

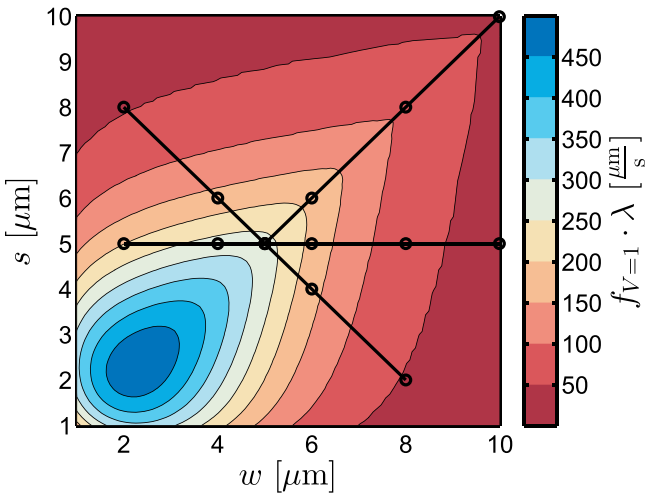

FIG. 6. Contour plot of simulations of the maximum magnetophoretic bead velocity, $f_{V=1} \cdot \lambda$, as function of w and s. The black lines and circles indicate the simulated data slices and parameters for the experimental data points in Fig. 5. A corresponding figure including all experimental values is given as supplementary Figure S2.[25] The simulations were done for M-270 beads with $\xi_{\text{M-270}} = 54\ \mu\text{m}^2/\text{Pa s}$, a rotating external magnetic field with $B_0 = 5\,\text{mT}$ and stripes with thickness $t_{\text{FM}} = 15\,\text{nm}$.

transportation velocity is limited by the time it takes for the bead to travel the larger pole separation, as a larger pole separation reduces the magnetic field gradient, cf. Fig. 1(c). This explains why a geometry with, e.g., $w = 10\,\mu\text{m}$, $s = 5\,\mu\text{m}$ is worse for bead transportation than a geometry with $w = 8\,\mu\text{m}$, $s = 8\,\mu\text{m}$, and why the maximum velocity decreases with decreasing w, for $w \leq 5\,\mu\text{m}$ and fixed $s = 5\,\mu\text{m}$ in Fig. 5(b).

The simulated data of Figs. 5(a) and 6 show that an optimal stripe period exists for a symmetric geometry. As the stripe period λ decreases, the distance between magnetic poles is reduced. This has two consequences: First, the magnetic field from the stripes is more confined, which increases the magnetic gradients and force. Second, decreasing the period modifies the magnetic field experienced by the bead from being dominated by the nearest pole to being a superposition of fields of similar magnitude from several poles. Then, the superposed magnetic field shows a more sinusoidal-like variation, see Fig. 1, which is better for bead transportation. However, the field also decreases in magnitude, which is bad for bead transportation. Thus, reducing the period first increases the magnetic gradient until the fields from several poles overlap and upon a further reduction of the period, the diminishing amplitude of the magnetic field variation eventually prevents transportation. For the M-270 beads, the theoretically optimal period is $\lambda_{\text{optimal}} \approx 5\,\mu\text{m}$, and thus the optimal stripe period is about three times the height of the bead center over the stripe array.

To further investigate the optimal period of a symmetric array of stripes, Fig. 7 shows the simulated maximum velocity $f_{V=1} \cdot \lambda$ as the function of the bead height, z, and the stripe period λ. Figure 7 shows that the maximum velocity generally increases for decreasing z and λ. However, in practice z and λ have lower limits due to the finite bead radius, chip fabrication limitations and the effect of shape anisotropy and demagnetization of the microstripes. Figure 7 is split into three regions by the lines $\frac{\partial \lambda f_{V=1}}{\partial z}|_{\lambda} = 0$ and $\frac{\partial \lambda f_{V=1}}{\partial \lambda}|_{z} = 0$. Region I (top region) is defined by $z > 0.32\lambda$. In this region, the stripe period is too small, and the amplitude of the magnetic field from the stripes is reduced. The maximum velocity can be increased by simply increasing the period to $\lambda = 3.1z$. For M-270 beads and a 100 nm thick protective coating of the chip, this corresponds to period of $\lambda = 4.7\,\mu\text{m}$, as also seen in Fig. 5(a). Similarly, region III (bottom region) is defined by $z < 0.13\lambda$. Here, the bead height is too low and beads are slowed down by the localized nature of the magnetic field from the stripes. The maximum bead velocity can thus be increased by using a thicker chip coating to increase the bead height to $z = 0.13\lambda$. Unless $0.13\lambda \leq z \leq 0.32\lambda$, the stripe system can easily be optimized by increasing the stripe period or the bead height z. For geometries in region II, the system can be optimized by

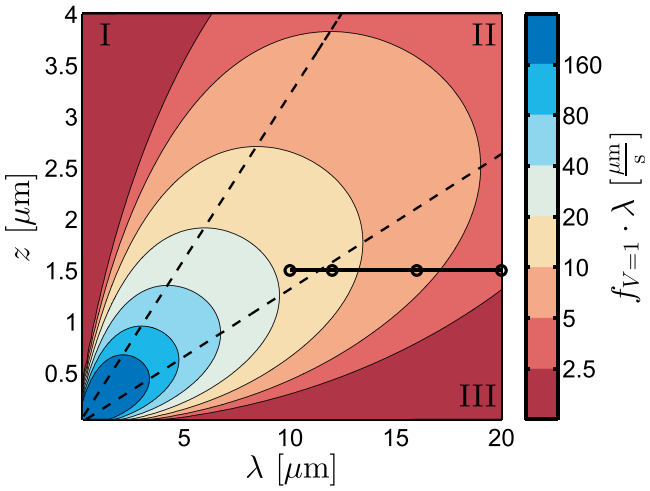

FIG. 7. Contour plot of the maximum bead velocity as function of stripe period, λ, and bead height z. The dashed lines correspond to $z = 0.13\lambda$ and $z = 0.32\lambda$. The data were calculated for $B_0 = 5$ mT, $t_{FM} = 1$ nm, $w = s = \lambda/2$, and $\xi_{M-270} = 54\ \mu m^2/Pa\ s$. The black lines and circles indicate the simulated data slices and parameters for the experimental data points in Fig. 5(a).

decreasing λ and/or z (while staying in region II) until practical limitations have been reached. Note that Fig. 7 is calculated for a low thickness of $t_{FM} = 1$ nm to prevent beads being trapped at the stripe edges.

To a very good approximation, the magnetic field from the stripes is proportional to t_{FM}. Increasing t_{FM} thus increases the amplitude of the magnetic field from the stripes, which can improve transportation velocities but also trap beads at the edge of the stripes if the external field is not strong enough. Further, increasing the thickness also lowers the pinning field from the antiferromagnetic layer. Thus, the optimal thickness is a complicated function of bead type, external fields, and the interaction between the magnetic layers. In the present study, a small total thickness of $t_{FM} = 15$ nm was used to reduce the number of beads being trapped at the edges of the magnetic stack.

B. Lower limit of bead size

For beads with a lower diameter of $2r = 1.3\ \mu$m, the optimal stripe width and spacing from Fig. 7 is $w = s \simeq 1\ \mu$m. This has two major practical disadvantages. First, UV-lithography fabrication techniques are diffraction limited to a line width of about $1\ \mu$m. Second, for such thin lines, shape anisotropy may decrease the overall magnetization of the stripes by rotating the magnetic moment towards the long axis of the stripe. For the stack used in the present study, this was observed when $w = s = 2\ \mu$m (Fig. S1[25]). Figure 8 shows the maximum bead velocity when the stripe width is limited to $1\ \mu$m as a function of the bead radius. The data in Fig. 8 were calculated assuming that no coating is present, i.e., $z = r$, and for a magnetophoretic mobility scaling as $\xi = \xi_{M-270}\ r^2/1.4\ \mu m^2$. As the bead height varies, the optimal period is given by $\lambda_{optimal} = 3.1z$. However, when $\lambda_{optimal} < 2\ \mu$m, the practical period is assumed to be $\lambda = 2\ \mu$m. Under these assumptions, the maximum bead velocity stays constant at $f_{V=1} \cdot \lambda \approx 500\ \mu$m/s until $r = 0.64\ \mu$m, below which the maximum velocity drops off rapidly. Thus, it will be difficult to maintain magnetophoretic transportation of beads at velocities of hundreds of μm/s when the beads have diameters much smaller than $1\ \mu$m by use of stripe geometries where the stripe width is limited to $w = 1\ \mu$m.

C. Sources of deviations between simulations and experiments

In Sec. IV, the measured velocities did not agree perfectly with the simulated velocities. Some of these discrepancies are due to measurement variations, see Sec. IV A, but other factors may also affect the results.

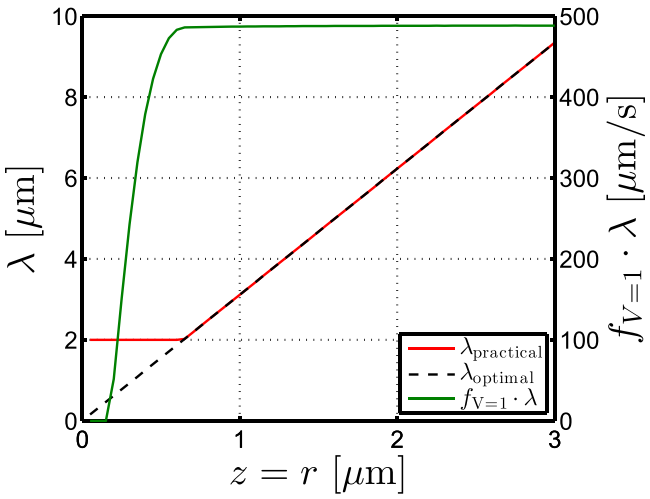

FIG. 8. Maximum magnetophoretic bead velocity, $f_{V=1} \cdot \lambda$, and the optimal period as function of the height z of the bead center over the stripe array, $\lambda_{\text{optimal}} = 3.1z$. The simulations were done with $t_{\text{FM}} = 15$ nm for a rotating external magnetic field with $B_0 = 5$ mT. The bead magnetophoretic mobility was assumed equal to $\xi = \xi_{\text{M-270}}\, r^2/1.4\ \mu\text{m}^2$.

First, the UV-lithography process was imperfect, and a slight overexposure during the photo lithography step led to stripes with widths slightly smaller than their nominal values. On average, we found the stripe width to be 0.24 μm lower than its nominal value. Correcting for this error would shift the measured velocities towards lower values of w compared to the nominal values used in Fig. 5. However, as the correction is much lower than 1 μm, it is insignificant compared to the observed differences.

Second, narrow stripes may be inhomogeneously magnetized due to shape anisotropy (see supplementary Figure S1[25]). This will effectively decrease their magnetic moment and thus lower the maximum obtainable magnetophoretic velocity compared to that obtained under ideal conditions in the simulations. Thus, experimental studies of peak-like features such as those in Fig. 5 are expected to show a broadening of the peak and a shift of the peak towards higher values of w compared to simulations carried out assuming homogeneously magnetized stripes. This agrees well with the observations in Fig. 5.

Third, when moving, the magnetic beads tend to line up behind each other. This formation could reduce the overall fluidic drag force on the beads and make the results depend on the period of the stripe geometry and the bead surface coverage such that the maximum magnetophoretic velocities obtained experimentally could be higher than those obtained in simulations. In our experiments, we have not observed any indications that this effect is important. Moreover, as the spacing between the beads along their direction of motion is given by the period of the stripe array, this effect would be expected to be of higher importance for low stripe periods and thus the peak shape in Fig. 5(c) for constant period should nominally not be affected by this effect.

Fourth, the simulations approximate the magnetic bead with a point dipole at its center and assume that the magnetic bead has a constant magnetic susceptibility. When the magnetic bead is located in a strong magnetic field gradient, the force on different parts of the bead may vary significantly and thus the assumption of a point dipole may be less justified. Generally, the assumption is valid when the magnetic field variation over the bead size is small compared to the magnetic field at the bead center, and this is not fulfilled for beads close to the edges of the stripes. However, the limiting factor for the maximum magnetophoretic bead velocity is the transportation in sections with weak magnetic field gradients and there the assumption is fulfilled. The approximation is therefore expected to have little impact on the result. For M-270 beads, the assumption of a constant magnetic susceptibility is well justified for fields below 10 mT.[23] From Fig. 1(b), it is observed that the magnetic field from the stripes at the bead

center for an M-270 bead in contact with the stripe array is below 5 mT and hence this assumption is well justified.

A comparison of the experimental results and simulations gives that the second factor is likely the most important one as it can at least qualitatively explain the differences observed in the observations for geometries with constant period (Fig. 5(c)). However, we note that the magnetic behavior of the stripe geometries is a quite complex function of both the stripe width and spacing.

VI. CONCLUSION

We have theoretically and experimentally investigated the magnetophoretic transportation properties of periodic microstripe array systems as the geometry of the permalloy microstripes was varied. Using a home-built setup and tracking algorithm, the maximum critical frequency for phase-locked motion of M-270 beads was systematically studied on thirteen chips with different stripe geometries. We found both experimentally and in simulations that the highest magnetophoretic velocities are obtained when the stripe array is formed from stripes with identical width and spacing. When this is fulfilled, the optimal stripe period λ is related to the height z of the center of the magnetic beads over the stripe array as $z/\lambda = 0.32$. Experimentally, for the optimal geometry, we found magnetophoretic velocities of M-270 beads of up to about 0.3 mm/s. We further theoretically investigated limitations of the presented stripe designs to transport magnetic beads with sizes approaching the nanoregime. For stripe arrays fabricated using conventional UV lithography, we found in simulations that the maximum obtainable magnetophoretic velocities are significantly lowered when the beads have diameters smaller than about 1 μm. Hence, the practical applicability of the presented approach may be limited to magnetic beads with sizes in the order of one micrometer or larger.

[1]S. Mornet, S. Vasseur, F. Grasset, and E. Duguet, "Magnetic nanoparticle design for medical diagnosis and therapy," J. Mater. Chem. **14**, 2161–2175 (2004).
[2]M. A. M. Gijs, F. Lacharme, and U. Lehmann, "Microfluidic applications of magnetic particles for biological analysis and catalysis," Chem. Rev. **110**, 1518–1563 (2010).
[3]A. M. Foudeh, T. Fatanat Didar, T. Veres, and M. Tabrizian, "Microfluidic designs and techniques using lab-on-a-chip devices for pathogen detection for point-of-care diagnostics," Lab Chip **12**, 3249–3266 (2012).
[4]S. Miltenyi, W. Müller, W. Weichel, and A. Radbruch, "High gradient magnetic cell separation with MACS," Cytometry **11**, 231–238 (1990).
[5]R. S. Molday, S. P. S. Yen, and A. Rembaum, "Application of magnetic microspheres in labelling and separation of cells," Nature **268**, 437–438 (1977).
[6]T. Deng, M. Prentiss, and G. M. Whitesides, "Fabrication of magnetic microfiltration systems using soft lithography," Appl. Phys. Lett. **80**, 461 (2002).
[7]J. W. Choi, C. H. Ahn, S. Bhansali, and H. T. Henderson, "A new magnetic bead-based, filterless bio-separator with planar electromagnet surfaces for integrated bio-detection systems," Sens. Actuators, B **68**, 34–39 (2000).
[8]M. Zborowski and J. J. Chalmers, "Rare cell separation and analysis by magnetic sorting," Anal. Chem. **83**, 8050–8056 (2011).
[9]A. G. J. Tibbe, B. G. De Grooth, J. Greve, P. A. Liberti, G. J. Dolan, and L. W. M. M. Terstappen, "Optical tracking and detection of immunomagnetically selected and aligned cells," Nat. Biotechnol. **17**, 1210–1213 (1999).
[10]N. Pekas, M. Granger, M. Tondra, A. Popple, and M. Porter, "Magnetic particle diverter in an integrated microfluidic format," J. Magn. Magn. Mater. **293**, 584–588 (2005).
[11]B. D. Plouffe, L. H. Lewis, and S. K. Murthy, "Computational design and optimization for microfluidic magnetophoresis," Biomicrofluidics **5**, 013413 (2011).
[12]M. Berger, J. Castelino, R. Huang, M. Shah, and R. H. Austin, "Design of a microfabricated magnetic cell separator," Electrophoresis **22**, 3883–3892 (2001).
[13]D. W. Inglis, R. Riehn, R. H. Austin, and J. C. Sturm, "Continuous microfluidic immunomagnetic cell separation," Appl. Phys. Lett. **85**, 5093 (2004).
[14]J. D. Adams, U. Kim, and H. T. Soh, "Multitarget magnetic activated cell sorter," Proc. Natl. Acad. Sci. U. S. A. **105**, 18165–18170 (2008).
[15]B. B. Yellen, R. M. Erb, H. S. Son, R. Hewlin, H. Shang, and G. U. Lee, "Traveling wave magnetophoresis for high resolution chip based separations," Lab Chip **7**, 1681–1688 (2007).
[16]L. Gao, N. J. Gottron, L. N. Virgin, and B. B. Yellen, "The synchronization of superparamagnetic beads driven by a micro-magnetic ratchet," Lab Chip **10**, 2108–2114 (2010).
[17]P. Li, A. Mahmood, and G. U. Lee, "Flow-enhanced nonlinear magnetophoresis for high-resolution bioseparation," Langmuir ACS J. Surf. Colloids **27**, 6496–6503 (2011).
[18]M. Donolato, B. T. Dalslet, and M. F. Hansen, "Microstripes for transport and separation of magnetic particles," Biomicrofluidics **6**, 024110 (2012).

[19]D. Holzinger, I. Koch, S. Burgard, and A. Ehresmann, "Directed magnetic particle transport above artificial magnetic domains due to dynamic magnetic potential energy landscape transformation," ACS Nano **9**, 7323–7331 (2015).
[20]A. Engel and R. Friedrichs, "On the electromagnetic force on a polarizable body," Am. J. Phys. **70**, 428–432 (2002).
[21]H. Bruus, *Theoretical Microfluidics*, Oxford Master Series in Condensed Matter Physics Vol. 18 (Oxford University Press, 2008).
[22]R. Wirix-Speetjens, W. Fyen, K. Xu, J. De Boeck, and G. Borghs, "A force study of on-chip magnetic particle transport based on tapered conductors," IEEE Trans. Magn. **41**, 4128–4133 (2005).
[23]G. Fonnum, C. Johansson, A. Molteberg, S. Morup, and E. Aksnes, "Characterisation of dynabeads by magnetization measurements and Mössbauer spectroscopy," J. Magn. Magn. Mater. **293**, 41–47 (2005).
[24]A. D. Henriksen, S. X. Wang, and M. F. Hansen, "On the importance of sensor height variation for detection of magnetic labels by magnetoresistive sensors," Sci. Rep. **5**, 12282 (2015).
[25]See supplemental material at http://dx.doi.org/10.1063/1.4934679 for the hysteresis loops of three chips and for a velocity contour plot with the experimental values indicated.